

Efficient production of syngas and lactic acid via CrB MBene/Cd_{0.8}Zn_{0.2}S Schottky heterojunction photocatalysis

Jiliang Ma^{a,1,*}, Aohua Li^{a,1}, Qiong Liu^b, Lei Chen^c, Min Hong^{c,*}, Runcang Sun^{a,*}

^a Liaoning Key Lab of Lignocellulose Chemistry and BioMaterials, Liaoning Collaborative Innovation Center for Lignocellulosic Biorefinery, College of Light Industry and Chemical Engineering, Dalian Polytechnic University, Dalian 116034, China

^b Institute of Analysis, Guangdong Academy of Sciences (China National Analytical Center, Guangzhou), Guangdong 510070, China

^c Centre for Future Materials and School of Engineering, University of Southern Queensland Springfield Central Queensland, 4300, Australia

ARTICLE INFO

Keywords:

Syngas
Lactic acid
Photocatalysis
CrB MBene
Schottky heterojunction

ABSTRACT

The photocatalytic conversion of biomass utilizing two-dimensional (2D) MBene as co-catalyst represents an exemplary approach for the sustainable production of syngas and lactic acid, capitalizing on the renewable resources of biomass carbon and solar energy. In this study, CrB MBene was synthesized via *in-situ* exfoliation in an HCl aqueous solution and subsequently integrated with Cd_{0.8}Zn_{0.2}S through an *in-situ* growth strategy, aiming to facilitate the photocatalytic co-production of lactic acid and syngas. Notably, the CZS/CrB-10 variant demonstrated a remarkable 12.3-fold enhancement in the hydrogen evolution rate (1746.6 μmol g⁻¹ h⁻¹) compared to standalone Cd_{0.8}Zn_{0.2}S, highlighting the exceptional co-catalytic efficiency and air stability of CrB MBene. Under optimal experimental conditions, the lactic acid yield and CO evolution rate attained 75.4 % and 917.8 μmol g⁻¹ h⁻¹, respectively. The incorporation of CrB MBene as a co-catalyst was found to significantly improve sunlight utilization, enhance the separation and transfer of photogenerated charge carriers, and mitigate the recombination of electrons and holes. This research underscores the potential of CrB MBene as a promising and cost-effective co-catalyst, with implications for advancing artificial photosynthetic systems and the integration of photocatalytic biomass refining with water splitting technologies.

1. Introduction

Syngas, a crucial intermediate in the production of various commercial chemicals such as ammonia, methanol, and synthetic hydrocarbon fuels, comprises a mixture of CO and H₂ [1–3]. Currently, syngas production predominantly relies on steam methane reforming or dry methane reforming processes, both of which involve substantial energy consumption and CO₂ emissions [4–6]. Given the urgent energy and environmental challenges, there is a pressing need for a sustainable and eco-friendly approach to syngas synthesis. Photocatalytic technology holds promising potential by integrating biomass refining with water reduction to H₂, thereby facilitating the production of syngas and high-value chemicals [7,8]. The ongoing advancements in photocatalytic systems for syngas production are expected to alleviate the energy crisis and mitigate environmental issues [9–11]. Central to achieving this goal is the design of photocatalysts featuring optimal structures and tunable redox properties. The incorporation of a

co-catalyst into the photocatalytic system, particularly when using a single material, emerges as an effective strategy [12–14]. This approach not only mitigates carrier recombination and enhances the capture of photogenerated electrons but also provides active sites for proton reduction reactions. While precious metals like Pt, Ag, and Au are recognized as effective co-catalysts for photocatalytic reactions, their high costs and scarcity limit their widespread application [15,16]. Consequently, there is an urgent need to develop efficient and cost-effective alternatives to precious metal co-catalysts, essential for the industrialization and commercialization of photocatalytic syngas production [17,18]. Such endeavors would not only advance the field but also contribute significantly to the transition towards a more sustainable energy landscape.

As an emerging class of 2D nanomaterial, MBenes represent a series of atomically thin layers of transition metal borides that similarities with MXenes, another class of 2D inorganic nanomaterials [19–21]. MBenes are obtained by selectively etching element A from the precursor MAB

* Corresponding authors.

E-mail addresses: jlma@dlpu.edu.cn (J. Ma), min.hong@unisq.edu.au (M. Hong), rcsun3@dlpu.edu.cn (R. Sun).

¹ Jiliang Ma and Aohua Li have contributed equally to this work

<https://doi.org/10.1016/j.apcatb.2025.125101>

Received 10 December 2024; Received in revised form 19 January 2025; Accepted 26 January 2025

Available online 26 January 2025

0926-3373/© 2025 Elsevier B.V. All rights are reserved, including those for text and data mining, AI training, and similar technologies.

phase (where M denotes an early transition metal, A signifies an A-group element, and B represents boron element). Specifically, Cr_2AlB_2 exhibits a layered crystal structure, anisotropic chemical bonds, anisotropic mechanical properties, and metallic conductivity. These characteristics suggest the feasibility of preparing 2D chromium borate nanosheets by selectively removing the Al layer from their 3D precursors, leveraging nanomaterials-based approaches. Zhang et al. were the first to demonstrate the potential to synthesize 2D CrB MBene from the Cr_2AlB_2 MAB phase, paving the way for its cost-effective production with high catalytic activity [22]. However, challenges remain in achieving complete etching or preventing oxidation of the 2D layer, primarily due to the continuous bonding between atoms B and A. This B-A bond, stemming from the reactivity of B, hinders the intercalation of foreign species between the 2D layers of the MAB phase, often leading to the dissolution of the entire phase rather than selective etching [23]. To address this, Alameda et al. reported incomplete acidic etching of MoAlB phase on 2D flat plates, resulting in various side phases, including oxides, in the final material [24]. Xiong et al. developed a hydrothermal-assisted NaOH solution etching method, successfully demonstrating its application in the synthesis of MoB MBene from MoAlB [25]. This innovative approach highlights the potential for advancing the synthesis of MBenes. However, the etching effect of alkaline solution remains limited, making it challenging to find a highly selective etching method that improves MBenes purity.

In this study, 2D CrB MBene was successfully synthesized via *in-situ* exfoliation in an aqueous HCl solution at ambient temperature. To date, there have been limited research reports documenting the experimental synthesis of CrB MBene. Photocatalytic technology relies on the redox oxidation-reduction reactions occurring on the surface of photocatalysts. Over the past few decades, numerous highly active, cost-effective, and robust semiconductor materials, such as $\text{g-C}_3\text{N}_4$, metal sulfides, and metal oxides, have emerged as candidates for photocatalytic applications [26]. Nevertheless, the rapid recombination of photoinduced electron-hole pairs remains a significant challenge in enhancing the performance of solar-driven photocatalysts. The $\text{Cd}_x\text{Zn}_{1-x}\text{S}$ solid solution, a prototypical ternary metal sulfide, has garnered significant attention due to its exceptional redox capabilities [27–29]. However, the standalone application of $\text{Cd}_x\text{Zn}_{1-x}\text{S}$ often suffers from severe photo-generated electron-hole recombination during photocatalytic processes, thereby impeding its practical deployment [30–32]. To address this issue, the incorporation of a co-catalyst into the photocatalytic system of $\text{Cd}_x\text{Zn}_{1-x}\text{S}$ represents an effective strategy. This approach not only mitigates carrier recombination and facilitates the capture of photo-generated electrons but also provides active sites for proton reduction reactions, thereby enhancing overall photocatalytic efficiency.

In this work, we employed a gentle exfoliation strategy to synthesize 2D CrB MBene, using Cr_2AlB_2 as the precursor material. We first investigated the oxidation process during exfoliation and the co-catalytic activity exhibited by the prepared 2D CrB MBene. Subsequently, we developed a CZS/CrB-x photocatalyst, assembled via electrostatic interactions, to explore the potential of 2D CrB MBene as an efficient co-catalyst for the visible-light-driven photocatalytic co-production of syngas and lactic acid from aqueous biomass solution. Additionally, it was elucidated the charge transfer mechanism occurring within the Schottky heterojunction through *in-situ* X-ray photoelectron spectroscopy (*in-situ* XPS). This work concurrently presents a promising avenue for the photocatalytic upgrading of aqueous biomass solution towards the production of high-value biomass chemicals and syngas.

2. Experimental section

2.1. Materials

Cr_2AlB_2 (212-type, 1–25 μm) was obtained from XFNANO Co., Ltd. (Jiangsu, China). $\text{Cd}(\text{CH}_3\text{COO})_2 \cdot 2 \text{H}_2\text{O}$ (analytical reagent, AR), Zn

$(\text{CH}_3\text{COO})_2 \cdot 2\text{H}_2\text{O}$ (AR), CrB (99.5 %), Cr_2O_3 (99.0 %), Al_2O_3 (99.0 %), B_2O_3 (98 %), *p*-phthalic acid (PTA, 99 %), thiourea (AR), and ethanol anhydrous (99.7 %), were procured from Shanghai Macklin Biochemical Co., Ltd. (Shanghai, China). HCl (37 % concentration), KOH (95 %), glucose (≥ 99 %), and lactic acid (≥ 98 % (T)) were purchased from Shanghai Aladdin Chemical Reagent Co., Ltd. (Shanghai, China). Tryptophan (Trp, 98 %), *p*-benzoquinone (BQ, 99 %), and ethylenediaminetetraacetic acid (EDTA, AR, 99.5 %) were all obtained from Sinopharm Chemical Reagent Co., Ltd. (Shanghai, China).

2.2. Preparation of 2D CrB-t MBene samples

0.5 g Cr_2AlB_2 samples were mixed with 40 mL of 1 M HCl and agitated for 2, 4, 8, or 24 h at room temperature, respectively, to exfoliate Al layers. After agitation, the suspension underwent ultrasonic treatment for 30 min, centrifugation at 5000 rpm for 10 min, and multiple rinses with deionized water to remove impurities. Finally, drying at 60 °C overnight, 2D CrB-t (t = 2, 4, 8, 24 h) MBene samples were collected.

2.3. Preparation of $\text{Cd}_{0.8}\text{Zn}_{0.2}\text{S}$, CZS/CrB-x, and the reference catalysts

0.8 mM $\text{Cd}(\text{CH}_3\text{COO})_2 \cdot 2\text{H}_2\text{O}$ and 0.2 mM $\text{Zn}(\text{CH}_3\text{COO})_2 \cdot 2 \text{H}_2\text{O}$ were dissolved in 10 mL of deionized water to yield system A. Following stirring for 12 h at room temperature, 1 mM of thiourea was added to system A. The mixture was heated in an autoclave at 120 °C for 12 h. Upon cooling to room temperature, the resulting orange $\text{Cd}_{0.8}\text{Zn}_{0.2}\text{S}$ samples were centrifuged and washed alternately with deionized water and ethanol, abbreviated as CZS.

The preparation of CZS/CrB-x composites was similar to the CZS protocol, with an additional step of incorporating 2D CrB-8 MBene. This included dispersing 0.2 g of 2D CrB-8 MBene in 20 mL deionized water, sonicating to form system B, and slowly mixing it with varying amounts (x mL) of system A. Following 12 h of stirring at room temperature and dissolving 0.1x (0.5, 1.0, 1.5, and 2.0) mM of thiourea, the mixture was treated in an autoclave at 120 °C for 12 h, yielding CZS/CrB-x composites (with x = 5, 10, 15, and 20).

The Pt served as the reference, a 5 wt% H_2PtCl_6 aqueous solution was employed for the *in-situ* photo-deposition of Pt on CZS, achieved through irradiation for 90 min. Similarly, CZS/ Al_2O_3 , CZS/ Cr_2O_3 , CZS/CrB, and CZS/ B_2O_3 samples were prepared using the preparation of CZS/CrB-10, substituting 2D CrB-8 MBene with Al_2O_3 , Cr_2O_3 , CrB, and B_2O_3 , respectively.

2.4. Photocatalytic synchronous production of syngas and lactic acid from glucose aqueous solution via different catalysts

The synchronous photocatalytic productions of syngas and lactic acid were performed using the Perfectlight PCX 50 C multi-channel photocatalytic reaction system (Beijing Perfectlight Technology Co., Ltd.). Typically, a quantity of 10 mg of photocatalyst and 600 mg of glucose were introduced into 30 mL of KOH solution, with various reaction conditions (including temperature, duration, and alkali concentration). After the reaction, the compositions of liquid and gaseous products were analyzed by high-performance liquid chromatography (HPLC) and gas chromatography (GC), respectively. Furthermore, the photocatalysts present in the system were filtered out and washed for the following test.

2.5. Poisoning experiments

10 mg of CZS/CrB-10, 600 mg of glucose, and 5 mmol of sacrificial agents (Trp, PTA, BQ, and EDTA) were introduced into 30 mL of a 3 M KOH solution. The reaction was performed under visible light at 60 °C for 3.5 h in the Perfectlight PCX 50 C system. Subsequently, the products were analyzed using the aforementioned methods.

2.6. Recycling experiment

The recycling experiments replicated the previous methodology. Each cycle was conducted by adding 10 mg CZS/CrB-10 and 600 mg glucose to 30 mL 3 M KOH solution, irradiating under visible light at 60 °C for 3.5 h in the Perfectlight PCX 50 C system, and analyzing products with HPLC and GC. After each cycle, the system was centrifuged at 3000 rpm for 10 min to separate CZS/CrB-10.

3. Results and discussion

3.1. Catalyst preparation and characterizations

The synthesis of 2D CrB-8 MBene and CZS/CrB-x is schematically presented in Fig. 1. Initially, the 2D CrB-8 MBene was synthesized through an *in-situ* exfoliation process in an HCl aqueous solution at room temperature. Then, different amounts of CZS were grown on the 2D CrB-8 MBene surface utilizing an *in-situ* growth strategy, resulting in the formation of CZS/CrB-x samples labeled as CZS/CrB-5, CZS/CrB-10, CZS/CrB-15, and CZS/CrB-20, respectively. The CZS/CrB-x was synthesized through an electrostatic self-assembly process. As shown in Fig. S1, $\text{Cd}_{0.8}\text{Zn}_{0.2}\text{S}$ exhibits a negative ζ potential of -23.9 mV, whereas the 2D CrB-8 MBene displays a positive ζ potential of 38.2 mV. Consequently, the negatively charged $\text{Cd}_{0.8}\text{Zn}_{0.2}\text{S}$ are attracted to the positively charged 2D CrB-8 MBene nanosheets, driven by electrostatic forces. This interaction facilitates the formation of the CZS/CrB-x photocatalyst.

X-ray diffraction (XRD) analysis (Fig. 2A) of 2D CrB-t MBene and CZS/CrB-x samples demonstrates structural changes following HCl exfoliation. Pristine Cr_2AlB_2 shows prominent diffraction peaks corresponding to the (001), (130), (111), and (041) planes (JCPDS No. 72–1847) at 30.0° , 39.1° , 44.0° , and 44.7° . Post-exfoliation, these peaks diminish significantly, indicating the removal of the Al layer. New peaks at 38.2° and 46.1° , attributed to the (021) and (130) planes of CrB (JCPDS No. 32–0277), confirm the formation of CrB, marking successful exfoliation. However, the persistence of original Cr_2AlB_2 peaks suggests incomplete exfoliation. Additionally, new peaks at 41.3° and 42.2° indicate the formation of Cr_2O_5 due to oxidation during the process, highlighting the need for further detailed investigation. To study morphological changes in MBene under different exfoliation times, we utilized scanning electron microscopy (SEM) and transmission electron microscopy (TEM). Fig. 2B highlights the bulk structure of pristine Cr_2AlB_2 . With 2 h of treatment in a 1 M HCl solution at room temperature, initial 2D lamellar structures start appearing (Fig. 2C). These structures become distinctly more defined by 4 h of exfoliation (Fig. 2D). Continuing the exfoliation to 8 h leads to complete removal of the internal Al layer, which results in a smoother and more uniform surface (Fig. 2E). However, extending the process to 24 h results in significant

degradation and disorganization of the surface structure (Fig. 2F). The energy-dispersive X-ray spectroscopy elemental mapping images of 2D CrB-24 MBene, revealing the coexistence of Cr, B, Al, and O elements, indicative of incomplete exfoliation of the Al layer and partial oxidation of the CrB MBene (Fig. 2G). The optimal condition for exfoliation, achieved at 8 h, shows minimal formation of oxide particles and a clean, well-ordered surface. Additionally, the high-resolution TEM (HRTEM) image of the optimally exfoliated 2D CrB-8 MBene (Fig. 2H) displays a well-defined layered structure with visible lattice fringes. The measurements indicate lattice spacings of 0.196 nm and 0.276 nm, corresponding to the (130) and (110) planes of CrB, respectively. These findings confirm the material's excellent crystallinity and structural precision, revealing the critical role of controlled exfoliation duration in achieving optimal material quality.

X-ray photoelectron spectroscopy (XPS) validated the successful exfoliation and oxidation of Cr_2AlB_2 . The Cr $2p_{1/2}$ spectrum from Cr_2AlB_2 (Fig. 3A) shows peaks at 586.4 eV (Cr-O) and 582.8 eV (Cr-B) [33,34]. The Cr $2p_{3/2}$ spectrum similarly displays peaks at 576.4 eV and 573.5 eV, confirming Cr-O and Cr-B bonds. For 2D CrB-8 MBene, these spectra exhibit shifts in peak intensities and ratios (Cr-O/Cr-B), indicating an increase in Cr_2O_5 content after HCl exfoliation (Table S1), corroborated by intensified Cr_2O_5 diffraction peaks in XRD results (Fig. 2A) at 41.3° and 42.2° . Additionally, the B $1s$ spectrum (Fig. 3B) splits into doublets for B-O (surface oxide B_2O_3) and B-Cr bonds, with binding energies shifting higher than in Cr_2AlB_2 , suggesting increased oxidation in 2D CrB-8 MBene [23]. The O $1s$ spectrum (Fig. 3C) shows three peaks at 532.7 eV ($\text{H}_2\text{O}_{\text{ads}}$), 531.7 eV ($\text{B}_2\text{O}_3/\text{CrB}(\text{OH})_x$), and 530.6 eV (Cr-oxides/ $\text{CrB}(\text{O})_x$), confirming O- and OH-terminations. The growing peak area ratio of O-Cr to O-B supports heightened O-termination and further Cr_2O_5 presence, indicating ongoing oxidation during exfoliation (Table S2). Fig. 3D illustrates that the peaks at 74.5 eV and 72.3 eV correspond to Al_2O_3 and Al metal, respectively. The absence of the Al metal peak verifies the complete removal of the Al layer, leaving a composite of CrB with oxides Cr_2O_3 , B_2O_3 , and Al_2O_3 in the exfoliated 2D CrB-8 MBene.

The SEM image of pure CZS shows a unique succulent-like microstructure (Fig. S2). This texture is preserved even after CZS is grown on 2D CrB-8 MBene, maintaining the 2D stacked structure (Figs. 4A and 4B). Additional needle-like structures on 2D CrB-8 MBene (Fig. 4C) indicate successful CZS deposition. Lattice spacings of 0.276 nm and 0.196 nm in CZS/CrB-10 align with CrB's (110) and (130) planes, while a 0.316 nm spacing matches CZS's (101) plane (Fig. 4D). Dislocations between these planes suggest a strong bond, forming a lattice-matched heterojunction. Energy-dispersive X-ray spectroscopy verifies the presence and uniform distribution of CZS components (Cd, Zn, S) on CrB (Fig. S3). As shown in Fig. 4E, the XRD pattern for CZS/CrB-10 features the main diffraction peaks of both 2D CrB-8 MBene and CZS. This dual peak presence is indicative of the successful synthesis of the composite

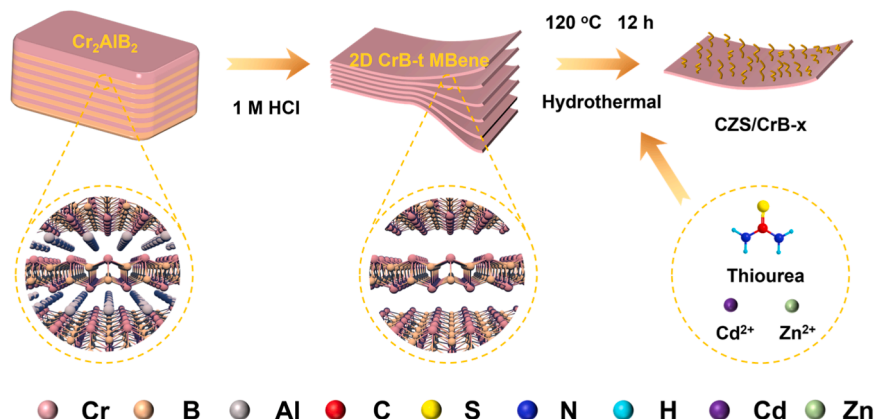


Fig. 1. Schematic illustration of fabricating CZS/CrB-x catalysts.

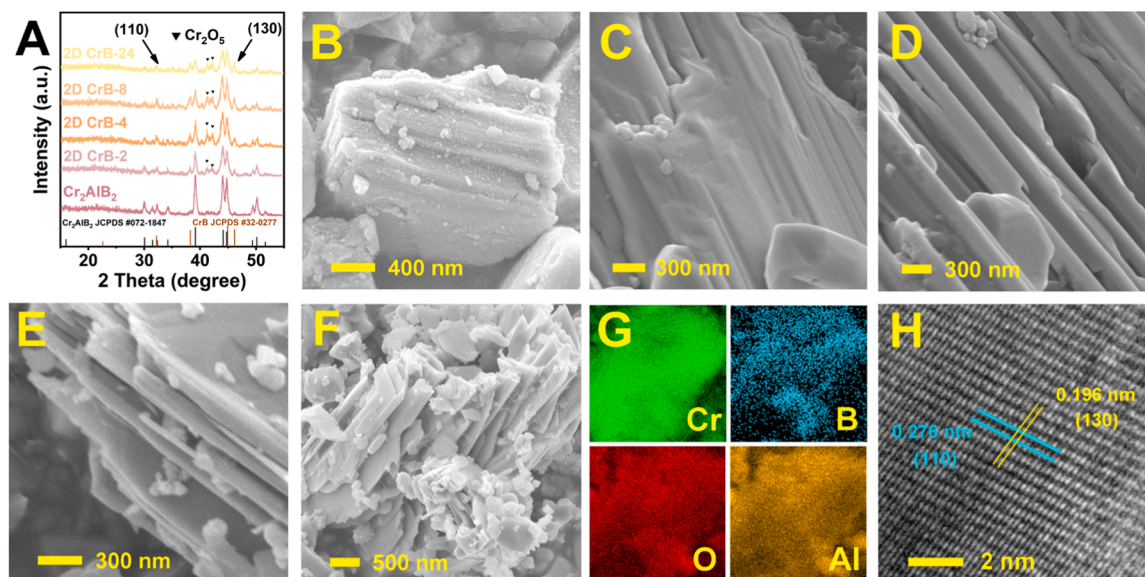


Fig. 2. XRD patterns of Cr_2AlB_2 , 2D CrB-*t* MBene derivatives with *t* = 2, 4, 8, and 24, denoting the time of exfoliations in 1 M HCl (A). SEM images of Cr_2AlB_2 , 2D CrB-*t* MBene derivatives with *t* = 2, 4, 8, and 24 (B-F). SEM EDS elemental mappings of 2D CrB-24 (G). HRTEM image of 2D CrB-8 MBene (H).

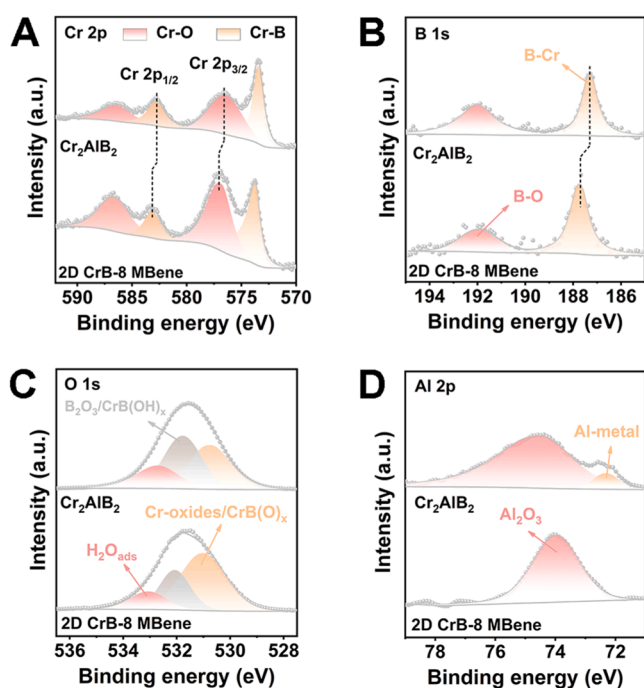


Fig. 3. XPS spectra of Cr 2p (A), B 1s (B), O 1s (C), and Al 2p (D) for Cr_2AlB_2 and 2D CrB-8 MBene.

material CZS/CrB-10.

XPS was utilized to explore the bonding state and chemical components of the materials. In the Cr 2p XPS spectra (Fig. 4F), two peaks at 586.7 eV (Cr-O) and 583.1 eV (Cr-B) for Cr 2p_{1/2}, with corresponding shifts for Cr 2p_{3/2} at 576.9 eV and 573.7 eV indicate changes in electron density and increased oxidation after hydrothermal treatment. Fig. 4G shows B 1s XPS spectra, fitted by doublets for B-O and B-Cr bonds, revealing an increased B-O to B-Cr peak area ratio post CZS loading, suggesting further oxidation of 2D CrB-8 MBene. A positive shift in the Cr-B bond binding energy supports an elevated oxidation state of 2D CrB-8 MBene. Fig. 4H depicts an increased peak area ratio of O-B to O-Cr, indicating enhanced OH-termination and oxidation. The Cd 3f XPS

spectra (Fig. 4I) display peaks for Cd 3d_{3/2} and Cd 3d_{5/2}, showing electron transfer from CZS to 2D CrB-8 MBene post hydrothermal treatment, indicative of heterojunction formation. Fig. 4J shows Zn 2p spectra with peaks at 1044.4 and 1021.4 eV for Zn 2p_{1/2} and Zn 2p_{3/2}. Fig. 4K identifies S 2p peaks associated with S²⁻, confirming successful preparation and further oxidation of CZS/CrB-10, showcasing effective heterojunction development.

3.2. Photocatalyst activity tests

These photocatalysts were evaluated for their ability to simultaneously produce syngas and lactic acid under visible light. The test conditions included a mixture of 600 mg glucose and 10 mg catalyst in 30 mL of 1 M KOH solution, irradiated for 3 h at 40°C. Fig. 5A compares the performance of different catalysts in producing syngas and lactic acid. It was found that CZS/CrB-10 exhibited a hydrogen evolution rate of 1746.6 μmol g⁻¹ h⁻¹, significantly surpassing bare CZS by approximately 1135%. The CZS/CrB-*x* system, leveraging CrB MBenes cocatalysts, significantly boosts photocatalytic activity for lactic acid production and CO evolution. This enhancement is linked to the synergistic effects between 2D CrB-8 MBene and CZS, reducing electrochemical impedance and boosting charge carrier mobility, thereby improving glucose oxidation selectivity. Notable byproducts include fructose and glyceraldehyde (Fig. S4). The CZS/CrB-10 variant achieves the highest lactic acid yield (33.1%) and CO evolution rate (1550.3 μmol g⁻¹ h⁻¹). However, increasing CZS content reduces photocatalytic activity due to a shielding effect that diminishes light absorption and carrier generation. Tests revealed that components of commercial Al₂O₃, Cr₂O₃, CrB, and B₂O₃, similar to CZS/CrB-10, show negligible impact on H₂ evolution, suggesting their limited role in the process (Fig. 5B). Control experiments with CZS combined with these components (CZS/Al₂O₃, CZS/Cr₂O₃, CZS/CrB, and CZS/B₂O₃) under identical conditions also displayed minimal H₂ evolution (Fig. 5C), highlighting the unique role of oxygenated groups on CrB MBene in enhancing H₂ performance [35]. To determine optimal conditions, we assessed the impact of KOH concentration on biomass conversion. At 0.1 M KOH, glucose predominantly isomerizes to fructose; however, this low alkali concentration does not favor lactic acid production [36]. Increasing KOH concentration enhances both lactic acid yield and glucose conversion, indicating further conversion of glucose and fructose to lactic acid at higher concentrations (Fig. 5D and S5). Investigating reaction time, the system

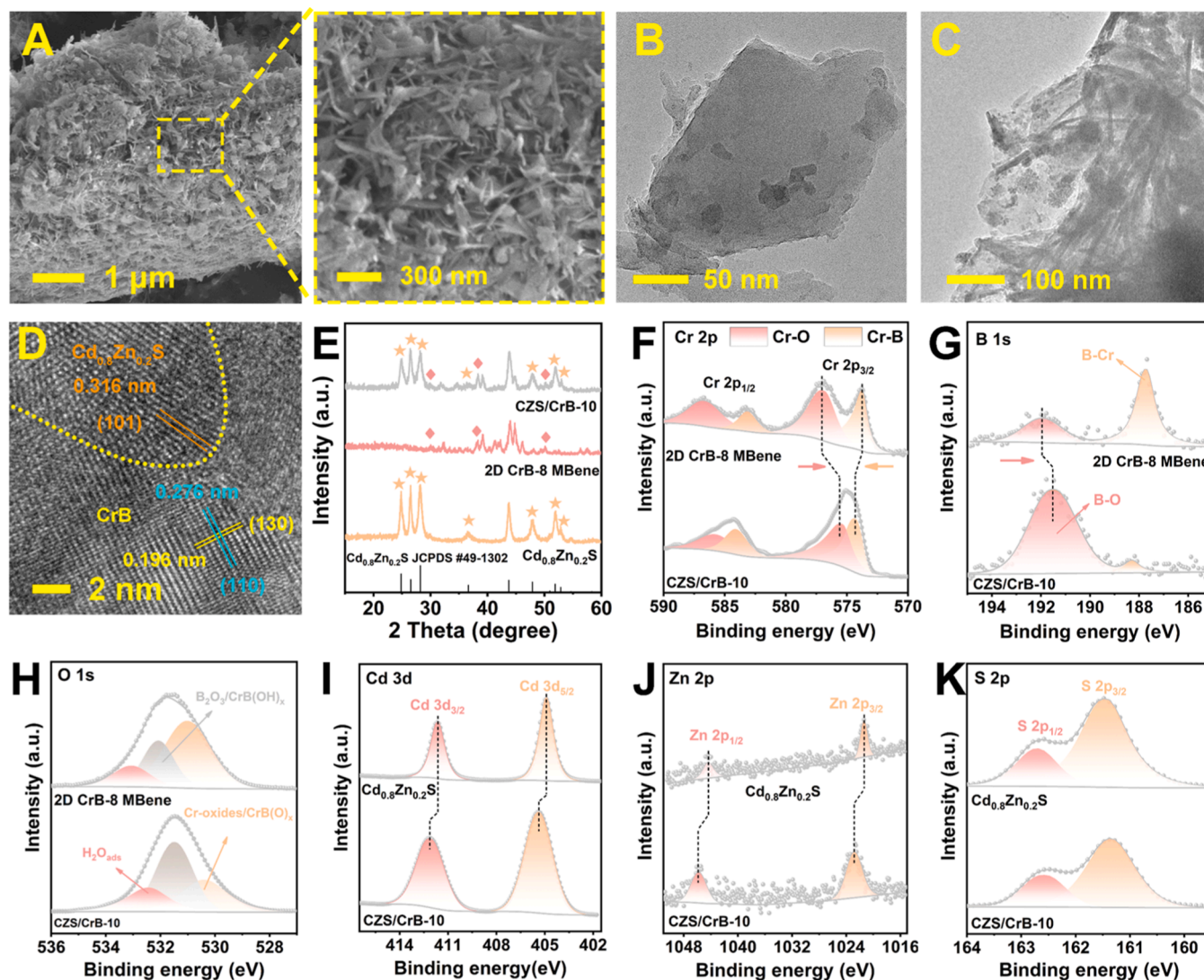


Fig. 4. SEM images of CZS/CrB-10 (A). TEM images of 2D CrB-8 MBene (B) and CZS/CrB-10 (C). HRTEM image of CZS/CrB-10 (D). XRD patterns of CZS, 2D CrB-8 MBene and CZS/CrB-10 (E). XPS spectra of Cr 2p (F), B 1s (G) and O 1s (H) for 2D CrB-8 MBene and CZS/CrB-10. XPS spectra of Cd 3d (I), Zn 2p (J) and S 2p (K) for CZS and CZS/CrB-10.

showed an increase in lactic acid yield over time, with peak CO and H₂ evolution rates observed at 210 min, displaying a CO ratio of 0.71 (Fig. 5E). Similarly, the glucose was isomerized to fructose in the early stages of the reaction (Fig. S6). Prolonging the irradiation time revealed consistent yield patterns for glyceraldehyde and CO. Increasing the temperature to 60°C maximizes lactic acid yield (75.4 %), while optimal CO and H₂ rates are achieved at 50°C, with a CO ratio of 1.56 (Fig. 5F). Byproduct yields indicated that higher temperatures favor the conversion of fructose to lactic acid (Fig. S7). Optimal conditions for this photocatalytic system involve 10 mg of CZS/CrB-10, 3 M KOH solution at 60°C, for a reaction time of 3.5 h. Control experiments confirm the critical roles of the photocatalyst, light, and alkali in the reaction (Fig. 5G), establishing a comprehensive framework for maximizing the photocatalytic efficiency of the CZS/CrB-x system. This catalyst also demonstrated good cycling stability over five runs (Fig. 5H), with XRD and XPS results showing no significant chemical changes (Fig. 5I and S8).

3.3. Catalytic mechanism of CZS/CrB-10

To understand the photoelectron chemical properties of the CZS/CrB-x photocatalysts, we conducted a series of characterizations

including ultraviolet-visible diffuse reflectance absorption spectra (UV-vis DRS), steady-state photoluminescence (PL), electrochemical impedance spectroscopy (EIS), transient photocurrent response, and time-resolved photoluminescence (TRPL). The UV-vis DRS indicated that CZS/CrB-x has red-shifted absorption edges compared to pure Cd_{0.8}Zn_{0.2}S, enhancing light absorption beyond 500 nm (Fig. 6A). Lower PL intensities for CZS/CrB-x compared to its components (Fig. 6B) suggest effective suppression of charge recombination. CZS/CrB-10 exhibited the most rapid charge separation, as evidenced by the strongest photocurrent responses and the smallest semicircles in EIS Nyquist plots (Fig. 6C and 6D). TRPL measurements revealed reduced average decay lifetimes across the samples, with CZS/CrB-10 showing the most significant decrease to 0.83 ns, indicating enhanced charge separation efficiency (Fig. 6E). Furthermore, linear sweep voltammetry (LSV) measurements were conducted to study the kinetic process. Fig. 6F displays that CZS/CrB-10 possesses a smaller overpotential for H₂ production as compared with bare Cd_{0.8}Zn_{0.2}S and 2D CrB-8 MBene, indicating a lower energy barrier of H₂ production with CZS/CrB-10. To investigate the underlying factors contributing to the remarkable photocatalytic performance of CZS/CrB-10, the electrochemical surface area (ECSA) of the photocatalysts was evaluated [37–39]. The double-layer capacitance (C_{dl}) of the electrocatalysts was determined from CV

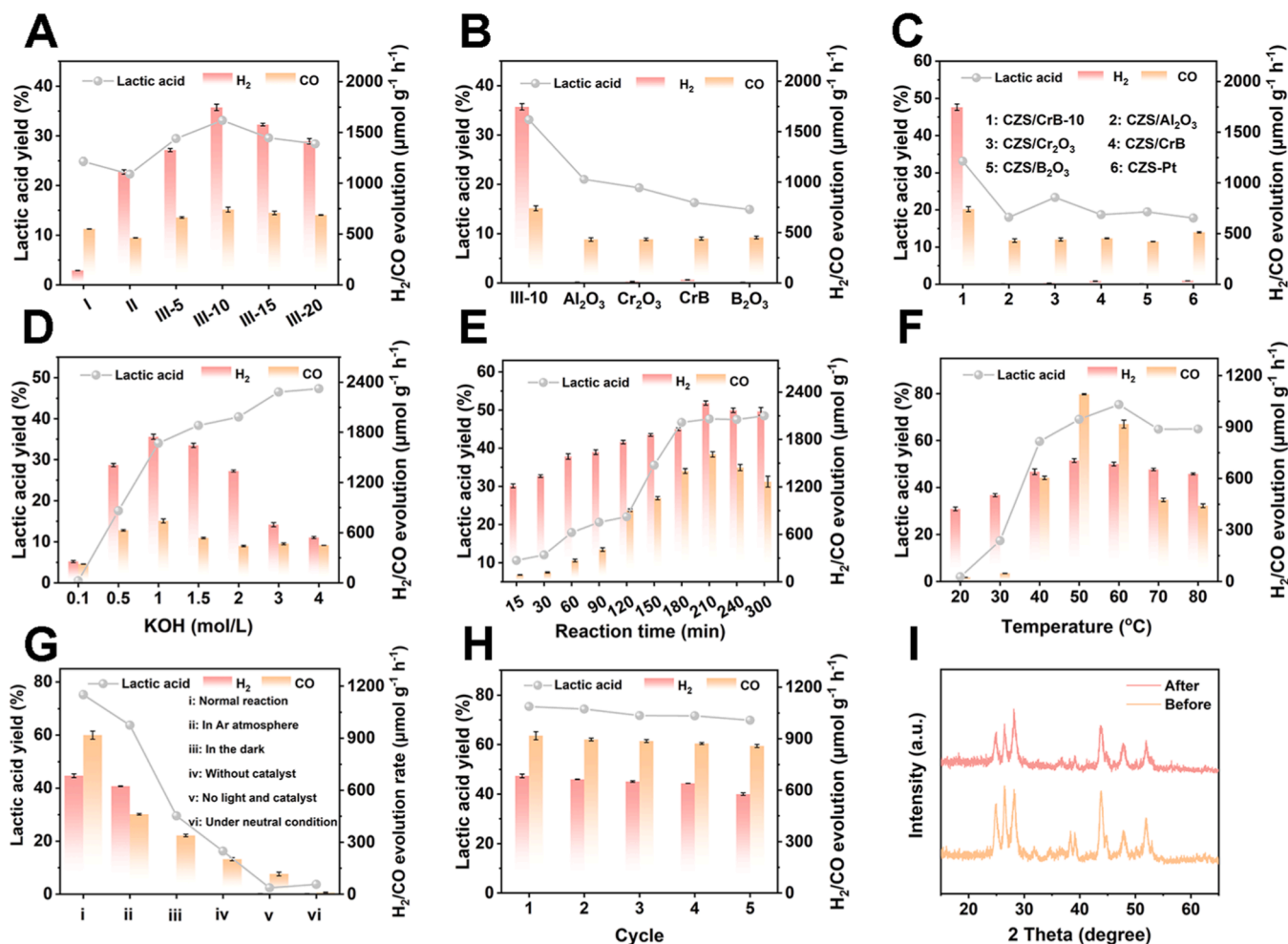


Fig. 5. (A) Photocatalytic conversion of glucose using different catalysts of CZS (I), 2D CrB-8 MBene (II), and CZS/CrB-x (III-x) with x = 5, 10, 15, and 20, representing the volume of thiourea added. (glucose: 600 mg, samples: 10 mg, KOH solution: 1 M, 30 mL, irradiation time: 180 min, reaction temperature: 40 °C). (B and C) Photocatalytic conversion of glucose using different samples under visible light irradiations showing the maximal efficiency of CZS/CrB-10 (III-10) (glucose: 600 mg, samples: 10 mg, KOH solution: 1 M, 30 mL, irradiation time: 180 min, reaction temperature: 40 °C). (D-G) Impacts of KOH concentration (glucose: 600 mg, CZS/CrB-10: 10 mg, KOH solution: 30 mL, irradiation time: 180 min, reaction temperature: 40 °C), irradiation time (glucose: 600 mg, CZS/CrB-10: 10 mg, KOH solution: 3 M, 30 mL, reaction temperature: 40 °C) and reaction temperatures (glucose: 600 mg, CZS/CrB-10: 10 mg, KOH solution: 3 M, 30 mL, irradiation time: 210 min) on the co-production of lactic and syngas. (G) Photocatalytic conversion of glucose using CZS/CrB-10 under different conditions. (H) Recycling test for the optimal CZS/CrB-10 (xylose: 600 mg, CZS/CrB-10: 10 mg, KOH solution: 3 M, 30 mL irradiation time: 210 min, reaction temperature: 50 °C). (I) The XRD patterns of fresh and recycled CZS/CrB-10.

curves recorded at varying scanning rates (Fig. S9). The calculated C_{dl} value for CZS/CrB-10, which is 0.329 mF cm^{-2} , exceeds those of CZS (0.279 mF cm^{-2}) and 2D CrB-8 (0.299 mF cm^{-2}). This finding suggests that CZS/CrB-10 possesses a greater number of exposed active sites.

Mott-Schottky analysis identified the conduction band potential of CZS at -0.75 V vs. NHE and a valence band at 1.92 V , confirming its n-type semiconducting nature (Fig. 7A). In addition, the VB of CZS was ascertained via XPS valence band analysis, revealing an E_{VB} of approximately 1.92 V (Fig. 7B). According to band theory, upon contact between photocatalysts, electrons can migrate from the photocatalyst with a lower work function (ϕ) to one with a higher ϕ . Consequently, ultraviolet photoelectron spectroscopy (UPS) was employed to determine the tested ϕ of CZS and 2D CrB-8 MBene. The cutoff energy (E_{cutoff}) of $\text{Cd}_{0.8}\text{Zn}_{0.2}\text{S}$ and 2D CrB-8 MBene were found to be 16.54 and 15.22 eV , respectively (Fig. 7C). Applying the formula $\phi = 21.20 \text{ eV} - E_{cutoff}$, where 21.20 eV represents the energy of UV excitation, the work functions of CZS and 2D CrB-8 MBene were estimated to be 4.66 and 5.98 eV relative to vacuum, respectively. Furthermore, the Fermi level (E_f) positions were calculated to be 0.22 eV for CZS and 1.54 eV for 2D CrB-8 MBene, using the equation $E_f = \phi - 4.44 \text{ eV}$, where 4.44 eV signifies

the difference between the vacuum level and NHE. Density Functional Theory (DFT) calculations indicated that the calculated ϕ of (130) crystal plane of 2D CrB-8 MBene and the (101) crystal plane of CZS were 5.418 and 4.114 eV , respectively (Fig. 7D-F). Although some deviation was observed between the tested and calculated ϕ , the trend remained consistent, indicating that the work function of 2D CrB-8 MBene is greater than that of CZS. Drawing upon the aforementioned results, the energy band structures of CZS/CrB-x are illustrated in Fig. 7G. The disparities in ϕ and E_f between the constituent materials instigate an e^- transfer process from CZS to CrB MBene, culminating in a redistribution of charges within the CZS/CrB-x composite and achieving a balanced E_f at the interface. The XPS spectra and band bending observed suggest a Schottky barrier formation at the CZS and CrB MBene interface, enhancing charge carrier separation under visible light. This barrier acts as an electron sink, preventing electron backflow into CZS, thus facilitating efficient H₂ evolution from H ions [40,41]. The positive shift in binding energies in *in-situ* XPS analyses further supports the migration of photogenerated electrons towards CrB MBene (Fig. 7H and S10). The integrated analyses demonstrate that the CZS/CrB-x heterostructure significantly enhances photocatalytic performance by optimizing charge

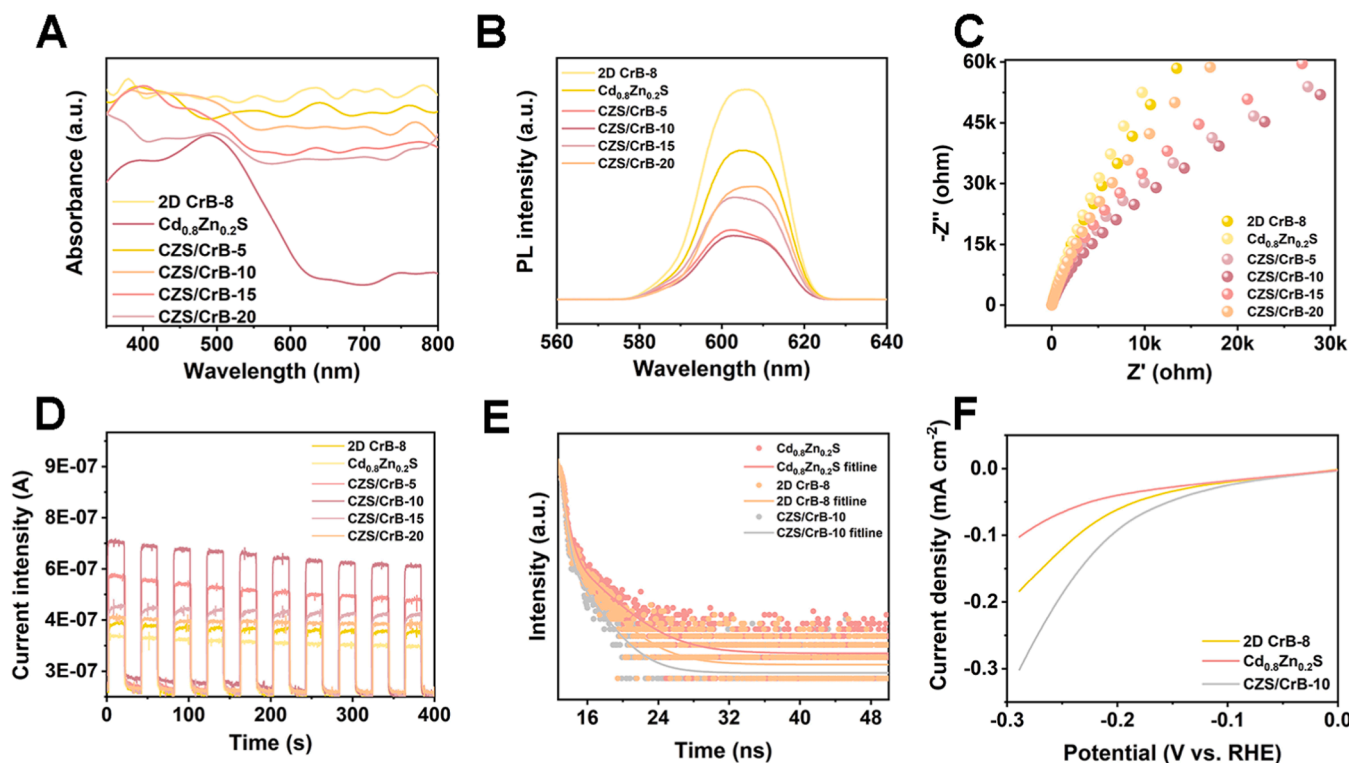


Fig. 6. (A) The UV-vis DRS of 2D-CrB-8h, $\text{Cd}_{0.8}\text{Zn}_{0.2}\text{S}$, and CZS/CrB-x. (B) The PL spectra of 2D-CrB-8h, $\text{Cd}_{0.8}\text{Zn}_{0.2}\text{S}$, and CZS/CrB-x. (C) EIS curves of 2D CrB-8 MBene, CZS, and CZS/CrB-x. (D) The photocurrent response plots of 2D CrB-8 MBene, CZS, and CZS/CrB-x. (E and F). TRPL decay curves and LSV curves of 2D CrB-8 MBene, CZS, and CZS/CrB-10.

carrier dynamics and lowering reaction barriers, making it a potent system for photocatalytic applications, particularly in hydrogen evolution.

The electron spin resonance (ESR) characterizations utilized various capture agents to identify the predominant oxidation-active species in CZS and CZS/CrB-10. The ESR/2,2,6,6-tetramethylpiperidine-*N*-oxyl (TEMPO) signal intensities for both $\text{Cd}_{0.8}\text{Zn}_{0.2}\text{S}$ and CZS/CrB-10 diminished after 5 min and 10 min of visible light irradiation, respectively, in comparison to their intensities in the dark. This indicates the presence of electrons (e^-) and holes (h^+) within the glucose-alkaline system under photocatalytic conditions. Notably, the ESR/TEMPO signal intensity for CZS/CrB-10 was significantly weaker than that of bare $\text{Cd}_{0.8}\text{Zn}_{0.2}\text{S}$. This result indicates an enhanced generation of photo-generated e^- and efficient charge separation due to the formation of heterojunctions between $\text{Cd}_{0.8}\text{Zn}_{0.2}\text{S}$ and 2D CrB-8 MBene (Figs. 8A and 8B). Additionally, the intensity of the DMPO- $\cdot\text{O}_2$ adduct signals for CZS/CrB-10 was more pronounced than that of $\text{Cd}_{0.8}\text{Zn}_{0.2}\text{S}$, suggesting an enhanced reducing capability (Fig. 8C). Similarly, the intensity of the TEMPONE- $^1\text{O}_2$ adduct signals for CZS/CrB-10 exhibited a significant increase, suggesting heightened generation of $^1\text{O}_2$ within the CZS/CrB-10 system (Fig. 8D). It is well known that $\cdot\text{OH}$ radicals are typically generated through the oxidation of surface-bound H_2O molecules on photocatalysts, with the oxidation potential of the $\text{H}_2\text{O}/\cdot\text{OH}$ reaction being reported at 2.37 V [42]. No signals corresponding to $\cdot\text{OH}$ were detected for either CZS or CZS/CrB-10, aligning with their respective band structures, as the valence band (VB) of CZS/CrB-10 did not reach the oxidation potential required for the $\text{H}_2\text{O}/\cdot\text{OH}$ reaction (Fig. S11). To further investigate the role of various oxidative active species in this photocatalytic system, a series of poisoning tests were conducted. In these tests, EDTA, Trp, and BQ were employed as scavengers to eliminate h^+ , $^1\text{O}_2$, and $\cdot\text{O}_2$, respectively. The yield of lactic acid and CO varied significantly under different scavenging conditions: 58.81 % and 737.7 $\mu\text{mol g}^{-1} \text{h}^{-1}$ (EDTA), 42.16 % and 535.2 $\mu\text{mol g}^{-1} \text{h}^{-1}$ (Trp), and 9.49 % and 143.9 $\mu\text{mol g}^{-1} \text{h}^{-1}$ (BQ). These results indicate that $\cdot\text{O}_2$

played a significant role in lactic acid yield (Fig. S12).

To elucidate the photocatalytic mechanism of the 2D CrB-8 cocatalyst in enhancing H_2 evolution in CZS systems, Density Functional Theory (DFT) calculations were performed, with computational details provided in the Supporting Information. Rational slab models for 2D CrB-8, CZS, and the CZS/CrB-10 heterojunction were constructed (Fig. S13-17). Analysis of the optimized structures revealed the Gibbs free energy (ΔG_{H}) for adsorbed hydrogen intermediates on these materials. For CZS, 2D CrB-8, and CZS/CrB-10, ΔG_{H} values were -1.41 , -1.35 , and -1.13 eV, respectively, highlighting the most catalytically active O sites in the CZS/CrB-10 heterojunction with a ΔG_{H} closest to the ideal zero for optimal H_2 evolution (Fig. 9A and B) [43]. The photocatalytic reaction process for converting glucose to lactic acid and CO via the CZS/CrB-10 heterojunction was also investigated using DFT. The reaction pathway involves multiple steps (Fig. 9C):

1. Glucose adsorption on CZS/CrB-10 ($\text{C}_6\text{H}_{12}\text{O}_6^*$, 0 eV).
2. Keto-enol tautomerization of glucose ($\text{C}_6\text{H}_{12}\text{O}_6^*$, 1.85 eV).
3. Isomerization to fructose ($\text{C}_6\text{H}_{12}\text{O}_6^*$, 1.85 eV).
4. Retro-aldol fragmentation of fructose to two C3 glyceraldehyde molecules ($\text{C}_3\text{H}_6\text{O}_3^*$, -0.86 eV).
5. Dehydration of glyceraldehyde to pyruvaldehyde ($\text{C}_3\text{H}_4\text{O}_2^*$, -2.6 eV).
6. Oxidation of pyruvaldehyde to pyruvic acid ($\text{C}_3\text{H}_4\text{O}_3^*$, -1.19 eV).
7. Reduction of pyruvic acid to lactic acid ($\text{C}_3\text{H}_6\text{O}_3^*$, -1.85 eV).

The formation pathway for CO parallels that of lactic acid up to step 4, beyond which oxidation of glyceraldehyde leads to CO and formic acid production, with a total activation energy of -0.86 eV. A proposed conversion mechanism based on experimental data and previous studies (Fig. S18) suggests that upon visible light irradiation, photo-excited electrons and holes generated in the CZS and 2D CrB-8 MBene react at the interface, facilitating H_2 evolution from water-derived protons [44, 45]. The advanced photocatalytic activities for H_2 and organic

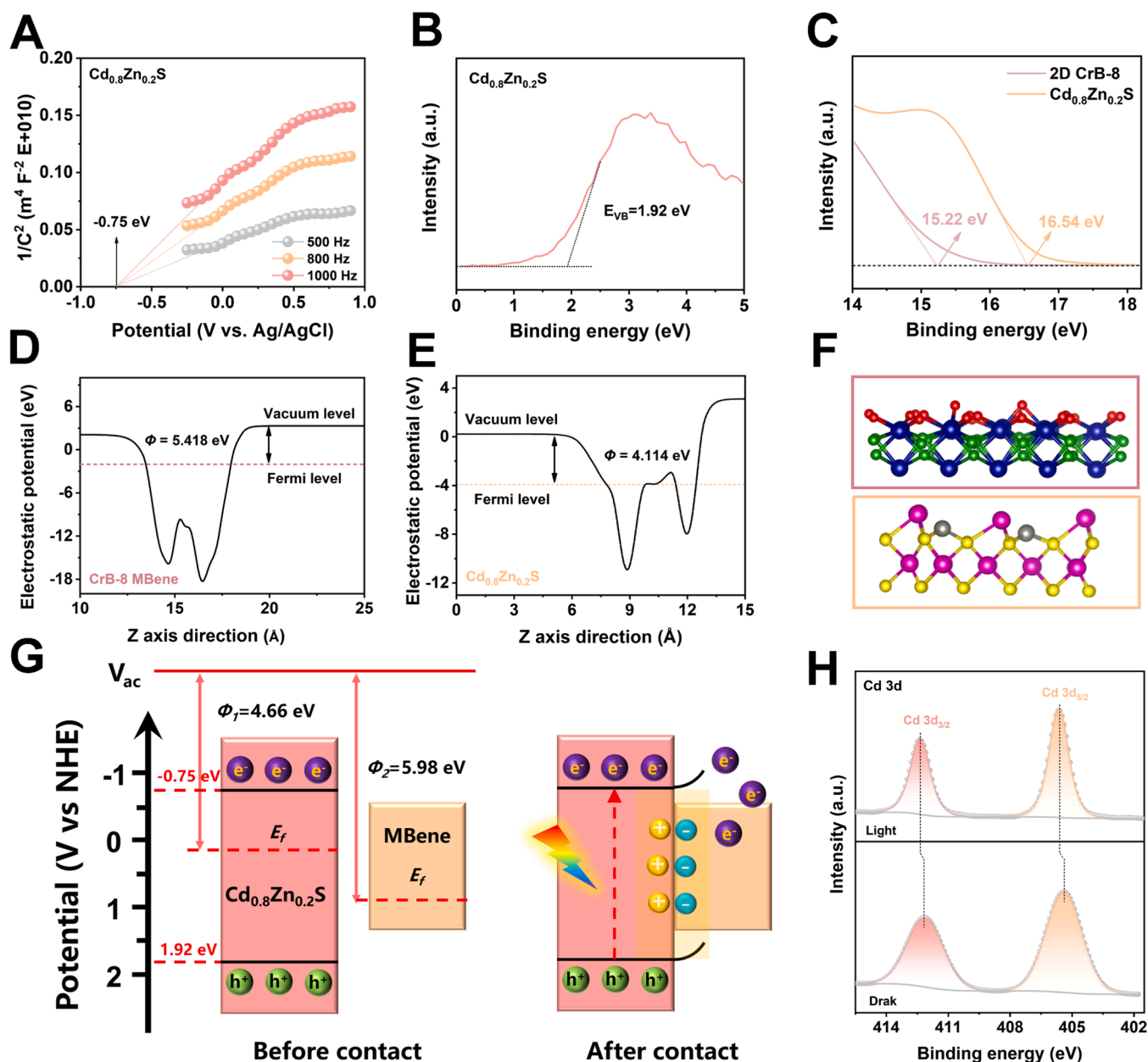


Fig. 7. The M-S plots (A) and valence band spectrum (B) of $\text{Cd}_{0.8}\text{Zn}_{0.2}\text{S}$. (C) The UPS of $\text{Cd}_{0.8}\text{Zn}_{0.2}\text{S}$ and 2D CrB-8 MBene. (D-F) The calculated work function and corresponding structural model of (130) plane of 2D CrB-8 MBene and (101) plane of $\text{Cd}_{0.8}\text{Zn}_{0.2}\text{S}$. (G) Schematic diagram of band structure. (H) The high-resolution *in-situ* XPS spectra of Cd 3d in CZS/CrB-10.

byproduct formation in the CZS/CrB-x system are significantly driven by the synergistic effects of component materials and their interaction at the molecular level, enhancing both hydrogen and valuable chemical production.

4. Conclusions

The successful preparation of 2D CrB MBene via an *in-situ* HCl aqueous solution exfoliation technique marks a significant advancement in material science. Through comprehensive analyses employing SEM, TEM, XRD, EDS, and XPS, we determined the optimal etching durations (2, 4, 8, and 24 h) necessary for effective material synthesis. It was observed that excessively prolonged exfoliation led to pronounced and disorganized surface degradation, affecting the material's structural integrity and performance. Building on this foundation, the CZS/CrB-x heterojunction was engineered by integrating CrB MBene with

$\text{Cd}_{0.8}\text{Zn}_{0.2}\text{S}$ using an *in-situ* growth strategy. This was specifically designed to enhance the photocatalytic co-production of syngas and lactic acid. Notably, the CZS/CrB-10 heterojunction exhibited outstanding photocatalytic performance, achieving a lactic acid yield of 75.4 %, and CO and H_2 evolution rates of $917.8 \mu\text{mol g}^{-1} \text{h}^{-1}$ and $683.8 \mu\text{mol}^{-1} \text{h}^{-1}$, respectively, under visible light irradiation in a 3 M KOH solution at 60°C . This configuration also demonstrated a 12.3-fold increase in the H_2 evolution rate compared to pure $\text{Cd}_{0.8}\text{Zn}_{0.2}\text{S}$ under an air atmosphere, illustrating the enhanced catalytic activity attributable to the heterojunction structure. Electrochemical Fermi level calculations and *in-situ* XPS analysis further confirmed the formation of a Schottky barrier, facilitating effective electron flow between $\text{Cd}_{0.8}\text{Zn}_{0.2}\text{S}$ and 2D CrB-8. This barrier is critical in enhancing charge separation and electron transport mechanisms, crucial for improved photocatalytic efficiency. The photocatalytic reaction mechanism for glucose oxidation to synthesize lactic acid and CO via the CZS/CrB-10 heterojunction was

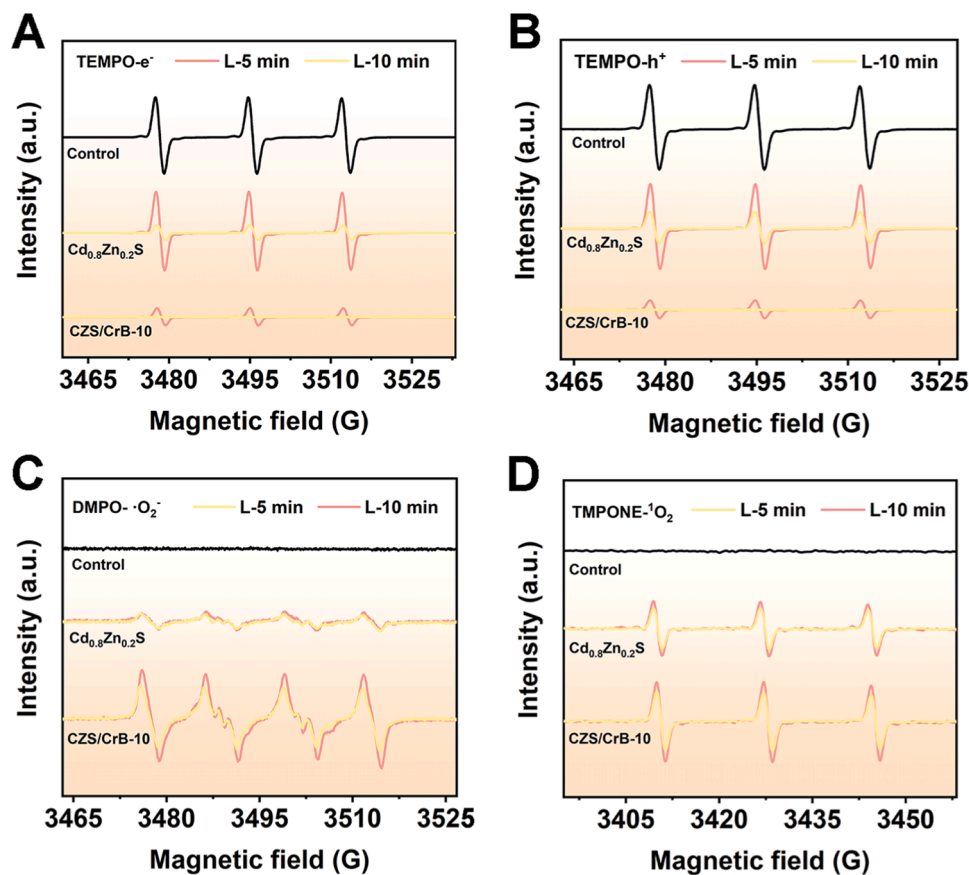


Fig. 8. TEMPO ESR spin-labeling of e^- (A) and h^+ (B), DMPO ESR spin-labeling of $\cdot O_2^-$ (C), TEMPONE ESR spin-labeling of 1O_2 (D).

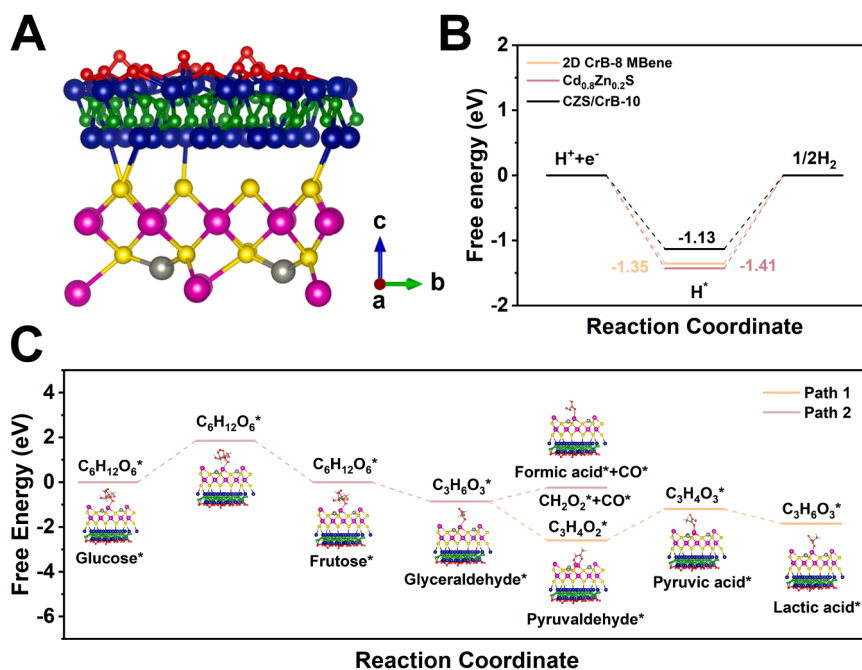


Fig. 9. (A) Atomic model of CZS/CrB-10 for adsorption proton calculation (Pink, gray, yellow, blue, green, red, and white spheres denote Cd, Zn, S, Cr, B, O, and H atoms, respectively). (B) Proton adsorption energy calculated for different models. (C) Calculated Gibbs free energy profile for the conversion of glucose into lactic acid and CO.

investigated through DFT calculations. These studies helped elucidate the stepwise transformation processes, providing a deeper understanding of the chemical dynamics at play. This study not only underscores the effectiveness of 2D CrB MBene as a co-catalyst but also highlights its potential in artificial photosynthetic systems for photocatalytic biomass upgrading coupled with water splitting. These findings pave the way for future research and development in sustainable energy solutions, leveraging the unique properties of 2D MBene materials.

Declaration of Competing Interest

The authors declare that they have no known competing financial interests or personal relationships that could have appeared to influence the work reported in this paper.

Acknowledgments

This work was supported by the National Natural Science Foundation of China (22378035, 22309032), Basic Scientific Research Project of Liaoning Provincial Department of Education (JYTZD2023028), Liaoning Province's "Xingliao Talent Plan" Youth Top Talents (XLYC2203010), Natural Science Foundation of Liaoning Province (2024-MS-173), Dalian Outstanding Young Scientific and Technological Talents (2022RY24), Australian Research Council (FT230100316 and IH200100035) and iLAUNCH Trailblazer Universities Program, Guangdong Basic and Applied Basic Research Foundation (2022A1515011737).

Appendix A. Supporting information

Supplementary data associated with this article can be found in the online version at [doi:10.1016/j.apcatb.2025.125101](https://doi.org/10.1016/j.apcatb.2025.125101).

Data Availability

Data will be made available on request.

References

- X.J. Wu, N.C. Luo, S.J. Xie, H.K. Zhang, Q.H. Zhang, F. Wang, Y. Wang, Photocatalytic transformations of lignocellulosic biomass into chemicals, *Chem. Soc. Rev.* 49 (2020) 6198–6223.
- A. Puga, *Coord. Chem. Rev.* 315 (2016) 1–66.
- G.Q. Zhao, X. Long, J. Zou, J. Hu, F.P. Jiao, Design of hollow nanostructured photocatalysts for clean energy production, *Coord. Chem. Rev.* 477 (2023) 214953.
- C.L. Wang, D. Astruc, Nanogold plasmonic photocatalysis for organic synthesis and clean energy conversion, *Chem. Soc. Rev.* 43 (2014) 7188–7216.
- R.Q. Fang, A. Dhakshinamoorthy, Y. Li, H. Garcia, Metal organic frameworks for biomass conversion, *Chem. Soc. Rev.* 49 (2020) 3638–3687.
- X.Y. Meng, J.J. Li, P. Liu, M.Y. Duan, J. Wang, Y.N. Zhou, Y.B. Xie, Z.H. Luo, Y. X. Pan, Long-term stable hydrogen production from water and lactic acid via visible-light-driven photocatalysis in a porous microreactor, *Angew. Chem. Int. Ed.* 62 (2023) e202307490.
- P. Stanley, A. Su, V. Ramm, P. Fink, C. Kimna, O. Lieleg, M. Elsner, J. Lercher, B. Rieger, J. Warnan, R. Fischer, Photocatalytic CO₂-to-syngas evolution with molecular catalyst metal-organic framework nanozymes, *Adv. Mater.* 35 (2023) 2207380.
- S.G. Xu, Y. Xiao, J.M. Li, W.Y. Zhang, C.W. Hu, Oligomer-first mechanism in the transformation of biomass derivatives selectively to produce D-lactic acid, *Chem. Eng. J.* 432 (2022) 134359.
- M. Wang, H.R. Zhou, F. Wang, Photocatalytic production of syngas from biomass, *Acc. Chem. Res.* 56 (2023) 1057–1069.
- W. Zhou, X. Wang, W.L. Zhao, N.J. Lu, D. Cong, Z. Li, P.G. Han, G.Q. Ren, L. Sun, C. C. Liu, W.Q. Deng, Photocatalytic CO₂ reduction to syngas using metallosalen covalent organic frameworks, *Nat. Commun.* 14 (2023) 6971.
- C.X. Dang, S.J. Wu, Y.H. Cao, H.J. Wang, F. Peng, H. Yu, Co-production of high quality hydrogen and synthesis gas via sorption-enhanced steam reforming of glycerol coupled with methane reforming of carbonates, *Chem. Eng. J.* 360 (2019) 47–53.
- L.L. Sun, N.C. Luo, Catalyst design and structure control for photocatalytic refineries of cellulosic biomass to fuels and chemicals, *J. Energy Chem.* 94 (2024) 102–127.
- Z.P. Huang, N.C. Luo, C.F. Zhang, F. Wang, Radical generation and fate control for photocatalytic biomass conversion, *Nat. Rev. Chem.* 6 (2022) 197–214.
- X.J. Wu, J.Q. Li, S.J. Xie, P.B. Duan, H.K. Zhang, J. Feng, Q.H. Zhang, J. Cheng, Y. Wang, Selectivity control in photocatalytic valorization of biomass-derived platform compounds by surface engineering of titanium oxide, *Chem* 6 (2020) 3038–3053.
- K.H. Chen, J.D. Xiao, J.J.M. Vequizo, T. Hisatomi, Y.W. Ma, M. Nakabayashi, T. Takata, N. Shibata, K. Domen, Overall water splitting by a SrTaO₂N-based photocatalyst decorated with an Ir-promoted Ru-based cocatalyst, *J. Am. Chem. Soc.* 145 (2023) 3839–3843.
- K.N. Li, S.S. Zhang, Y.H. Li, J.J. Fan, K.L. Lv, MXenes as noble-metal-alternative cocatalysts in photocatalysis, *Chin. J. Catal.* 42 (2021) 3–14.
- H. Saito, T. Higashi, T. Higashi, T. Sugimoto, Beyond reduction cocatalysts: critical role of metal cocatalysts in photocatalytic oxidation of methane with water, *Angew. Chem. Int. Ed.* 62 (2023) e202306058.
- Y. Jiao, Y. Zheng, M. Jaroniec, S.Z. Qiao, Design of electrocatalysts for oxygen- and hydrogen-involving energy conversion reactions, *Chem. Soc. Rev.* 44 (2015) 2060–2086.
- T.J. Xu, Y.H. Wang, Z.Z. Xiong, Y.T. Wang, Y.T. Zhou, X.F. Li, A rising 2D star: novel MBenes with excellent performance in energy conversion and storage, *Nano-Micro Lett.* 15 (2022) 6.
- W.Q. Qian, S.W. Xu, X.M. Zhang, C.B. Li, W.Y. Yang, C. Bowen, Y. Yang, Differences and similarities of photocatalysis and electrocatalysis in two-dimensional nanomaterials: strategies, traps, applications and challenges, *Nano-Micro Lett.* 13 (2021) 156.
- G. Murali, J. Reddy, Modigunta, Y. Park, J.H. Lee, J. Rawal, S.Y. Lee, I. In, S. J. Park, A review on MXene synthesis, stability, and photocatalytic applications, *ACS Nano* 16 (2022) 13370–13429.
- H.M. Zhang, H.M. Xiang, F.Z. Dai, Z.L. Zhang, Y.C. Zhou, First demonstration of possible two-dimensional MBene CrB derived from MAB phase Cr₂AlB₂, *J. Mater. Sci. Technol.* 34 (2018) 2022–2026.
- D. Bury, M. Jakubczak, M. Purbayanto, Wet-chemical etching and delamination of MoAlB into MBene and its outstanding photocatalytic performance, *Adv. Funct. Mater.* 33 (2023) 2308156.
- L.T. Alameda, P. Moradifar, Z.P. Metzger, Topochemical deintercalation of Al from MoAlB: stepwise etching pathway, layered intergrowth structures, and two-dimensional MBene, *J. Am. Chem. Soc.* 140 (2018) 8833–8840.
- W. Xiong, X.Y. Feng, Y. Xiao, T. Huang, X.Y. Li, Z.C. Huang, S.H. Ye, Y.L. Li, X. Z. Ren, X.Z. Wang, X.P. Ouyang, Q.L. Zhang, J.H. Liu, Fluorine-free prepared two-dimensional molybdenum boride (MBene) as a promising anode for lithium-ion batteries with superior electrochemical performance, *Chem. Eng. J.* 446 (2022) 137466.
- A. Holm, M. Hamandi, F. Simonet, B. Jouguet, F. Dappozze, C. Guillard, Impact of rutile and anatase phase on the photocatalytic decomposition of lactic acid, *Appl. Catal. B-Environ. Energy* 253 (2019) 96–104.
- K. Yu, T.Y. Zhang, Y.M. Wang, Anchoring Co₃O₄ on CdZnS to accelerate hole migration for highly stable photocatalytic overall water splitting, *Appl. Catal. B-Environ. Energy* 324 (2023) 122228.
- L.L. He, X.H. Zeng, H. Chen, L. Zhao, Z.H. Huang, D.H. Wang, X. He, W. Fang, X. Du, W.X. Li, A hybrid photocatalytic system splits atmospheric water to produce hydrogen, *Adv. Funct. Mater.* 34 (2024) 2313058.
- P. Su, D. Zhang, M.H. Zhu, Re-usable Cd_{0.9}Zn_{0.1}S-ZnO@C/PVDF piezo-photocatalytic film with exceptional hydrogen evolution capability triggered by the synergetic advantages of piezoelectricity and S-Scheme heterojunction, *J. Energy Chem.* 96 (2024) 164–176.
- B. Su, M. Zheng, W. Lin, X.F. Lu, D. Luan, S.B. Wang, X.W. Lou, S-Scheme Co₉S₈@Cd_{0.8}Zn_{0.2}S-DETA hierarchical nanocages bearing organic CO₂ activators for photocatalytic syngas production, *Adv. Energy Mater.* 13 (2023) 2203290.
- B. Su, H.W. Huang, Z.X. Ding, M.B.J. Roefiaers, S.B. Wang, J.L. Long, S-scheme CoTiO₃/Cd_{0.5}Zn_{0.49}S₁₀ heterostructures for visible-light driven photocatalytic CO₂ reduction, *J. Mater. Sci. Technol.* 124 (2022) 164–170.
- B.F. Li, W.J. Wang, Z.Y. Wang, B. Su, Y.D. Hou, Z.X. Ding, S.B. Wang, All-solid-state direct S-scheme NiTiO₃/Cd_{0.5}Zn_{0.5}S heterostructures for photocatalytic hydrogen evolution with visible light, *J. Mater. Chem. A* 9 (2021) 10270–10276.
- M.H. Wu, M. Gao, S.Q. Qu, Y.F. Liu, W.P. Sun, C. Liang, X. Zhang, Z.L. Li, Y. X. Yang, H.G. Pan, LiBH₄ hydrogen storage system with low dehydrogenation temperature and favorable reversibility promoted by metallocene additives, *J. Energy Storage* 72 (2023) 108679.
- E. Benko, A. Wyczesany, A. Bernasik, T.L. Barr, E. Hoope, CBN-Cr/Cr₂C₂ composite materials: chemical equilibria, XPS Investig. *Ceram. Int.* 26 (2000) 545–550.
- B. Montejo-Valencia, M. Curet-Arana, Periodic DFT study of the opening of fructose and glucose rings and the further conversion of fructose to trioses catalyzed by M-BEA (M = Sn, Ti, Zr, or Hf), *J. Phys. Chem. C* 123 (2019) 3532–3540.
- L. Meng, L. Yan, F. Vines, F. Illas, Effect of terminations on the hydrogen evolution reaction mechanism on Ti₃C₂ MXene, *J. Mater. Chem. A* 11 (2023) 6886–6900.
- H.Y. Pang, T. Gao, W.K. Zhao, L. Liu, E.Z. Liu, H.Y. Wen, T. Sun, Construction of MoSe₂/Ni₃Se₂/NF Schottky heterojunction as electrocatalyst for water splitting and electrochemical oxidation for sulfur recovery, *Fuel* 374 (2024) 132532.
- T. Sun, C.X. Li, Y.P. Bao, J. Fan, E.Z. Liu, S-Scheme MnCo₂S₄/g-C₃N₄ heterojunction photocatalyst for H₂ production, *Acta Phys. -Chim. Sin.* 39 (2023) 2212009.
- T. Sun, J. Wang, C.T. Qiu, X. Ling, B.B. Tian, W. Chen, C.L. Su, B. N codoped and defect-rich nanocarbon materials as a metal-free bifunctional electrocatalyst for oxygen reduction and evolution reactions, *Adv. Sci.* 5 (2018) 1800036.
- H. Zhao, L. Wang, G.H. Liu, Y.T. Liu, S.Q. Zhang, L.H. Wang, X.B. Zheng, L.Y. Zhou, J. Gao, J.F. Shi, Y.J. Jiang, Hollow Rh-COF@COF S-scheme heterojunction for

- photocatalytic nicotinamide cofactor regeneration, *ACS Catal.* 13 (2023) 6619–6629.
- [41] S. Jin, Z. Shi, R.G. Wang, Y.T. Guo, L.B. Wang, Q.K. Hu, K. Liu, N. Li, A.G. Zhou, 2D MoB MBene: an efficient co-catalyst for photocatalytic hydrogen production under visible light, *ACS Nano* 18 (2024) 12524–12536.
- [42] J. Yang, L. Yang, M. Fang, L. Li, F. Fu, H. Xu, M.G. Li, X.M. Fan, A compact Z-scheme heterojunction of BiOCl/Bi₂WO₆ for efficiently photocatalytic degradation of gaseous toluene, *J. Colloid Interface Sci.* 631 (2023) 44–54.
- [43] Z.X. Fan, Y.L. Cai, Z.Y. Yang, X. Zhang, R.W. Shao, S.X. Zhong, L.H. Zhao, D. Liu, S. Bai, Integrating CO₂ reduction, H₂O oxidation and H₂ evolution catalysts into a dual S-scheme artificial photosynthetic system for tunable syngas production, *Appl. Catal. B-Environ. Energy* 351 (2024) 123979.
- [44] A.H. Li, J.L. Ma, M. Hong, R.C. Sun, Enhanced CeO₂ oxygen defects decorated with AgInS₂ quantum dots form an S-scheme heterojunction for efficient photocatalytic selective oxidation of xylose, *Appl. Catal. B-Environ. Energy* 348 (2024) 123834.
- [45] S.Y. Wang, A.H. Cheng, F.H. Liu, J.J. Zhang, T. Xia, X. Zeng, W. Fan, Y. Zhang, Catalytic conversion network for lignocellulosic biomass valorization: a panoramic view, *Ind. Chem. Mater.* 1 (2023) 188–206.